# Time propagation and spectroscopy of Fermionic systems using a stochastic technique

Kai Guther,[1, *] Werner Dobrautz,[1, †] Olle Gunnarsson,[1, ‡] and Ali Alavi[1, 2, §]

[1] *Max Planck Institute for Solid State Research, Heisenbergstraße 1, 70569 Stuttgart, Germany*
[2] *University Chemical Laboratory, Lensfield Road, Cambridge, CB2 1EW, U.K.*

We present a stochastic method for solving the time-dependent Schrödinger equation, generalizing a ground state full configuration interaction Quantum Monte Carlo method. By performing the time-integration in the complex plane close to the real time axis, the numerical effort is kept manageable and the analytic continuation to real frequencies is efficient. This allows us to perform *ab initio* calculation of electron spectra for strongly correlated systems. The method can be used as cluster solver for embedding schemes.

*Introduction.* The time evolution of a closed interacting electronic system, having been prepared in a well-defined but entangled non-stationary state, is of considerable interest to a broad range of fields. This includes many types of electronic spectroscopy such as photoemission (PE) and inverse photoemission (IPE) [1–3] , core-level [4, 5] and optical spectroscopies, as well as the field of non-equilibrium dynamics [6], including dynamics in driven, time-dependent, external fields. In solid-state physics, such electronic spectroscopies play a leading role in providing information on the electronic structure of the material. In weakly-correlated materials, the GW-approximation provides a viable theoretical tool for calculating excitation energies [1, 7]. In strongly-correlated materials, however, theoretical studies are often limited to model systems such as the Hubbard [8] or Anderson [9] models. Efficient methods have been developed for studying such models.[10, 11] However, it is not clear how these methods can be generalized to *ab initio* calculations. Here we show how this can be achieved using a time evolution method stochastically applied to *ab initio* Hamiltonians.

Time evolution of quantum systems is a notoriously difficult problem owing to the existence of a severe dynamical sign problem. For electronic systems there is another difficult sign-problem due to its fermionic nature. Fundamentally, we are required to integrate the time-dependent Schrödinger equation for a many-electron system for long times. Methods based on deterministic wavefunction propagation, such as the Crank-Nicolson method [12], or Lanczos recursion [13, 14], suffer from severe memory requirements. Quantum Monte Carlo methods (especially quantum lattice methods) typically work in imaginary frequency space [10, 11], followed by analytic continuation to to real frequencies. The analytic continuation is numerically highly ill-conditioned, and maximum entropy (MaxEnt) methods [15, 16] are usually employed. Although spectral features close to the Fermi energy can be obtained rather accurately, features further away, e.g., satellites, are smeared out (see appendix [17]). Such satellites, however, can contain a wealth of information about the dynamics of the system.

In ab initio models these problems are further exacerbated by the large range of energies spanned by the basis set (over numerous Hartrees) and the huge Hilbert spaces owing to the large number of virtual orbitals.

In this letter we present an approach to this problem. We present a real-time generalization of an algorithm for calculating fermionic ground states using imaginary-time propagation. This involves the introduction of a second-order time propagator, which is implemented in a stochastic manner. This approach yields accurate time-correlation functions, but the computational cost increases exponentially, as the undamped time-evolving wave functions explores the available (exponentially large) Hilbert space. To ameliorate this problem, we introduce an adaptive variable-phase time-step into the propagator, which leads to a propagation in the complex plane close to the real time axis. This results in a slow damping, which keeps the computational cost essentially fixed (similar to a ground state calculation). Nevertheless, this gives phase information about the wave function and yields oscillatory time-correlation functions. We have developed a MaxEnt scheme, which performs analytic continuation from an arbitrary path in complex time space to real frequencies. This provides spectral functions over a broad energy range. We apply the method to benchmark systems for which numerically exact results are available, and show that these are reproduced to high accuracy at a fraction of the cost. Then we apply the algorithm to ab initio (atomic and molecular) systems, where comparison is made with experiment.

In *ab initio* calculations for solids, this method could be used as a cluster solver in embedding schemes like dynamical cluster approximation[10].

*Real-time evolution.* Given a Hamiltonian $\hat{H}$ and an initial wave function $|\Psi(0)\rangle$, we wish to solve the time-dependent Schrödinger equation:

$$i\frac{\partial}{\partial t}|\Psi(t)\rangle = \hat{H}|\Psi(t)\rangle \qquad (1)$$

$|\Psi(t)\rangle$ gives information about various spectroscopic properties. We can see this by considering the inverse

photoemission spectrum $A_{ii}(\omega)$

$$A_{ii}(\omega) = \sum_n |\langle\Psi_n^{N+1}|c_{i\sigma}^\dagger|\Psi_0^N\rangle|^2\delta(\omega - E_n^{N+1} + E_0^N + \mu),$$
(2)

where $c_{i\sigma}^\dagger$ adds an electron with spin $\sigma$ to orbital $i$ in the ground state $|\Psi_0^N\rangle$ with $N$ electrons. Here $|\Psi_n^{N+1}\rangle$ is the $n$th excited state of the $(N+1)$-electron system. $E_0^N$ and $E_n^{N+1}$ are the corresponding energies and $\mu$ is the chemical potential. The formal solution of Eq. (1) is $|\Psi(t)\rangle = \exp(-i\hat{H}t)|\Psi(0)\rangle \equiv \hat{U}(t)|\Psi(0)\rangle$. The spectrum is then given by

$$A_{ii}(\omega) = \frac{1}{\pi}\mathrm{Im}\left[-\mathrm{i}\int_0^\infty dt e^{i[\omega+i0^+ + E_0(N)+\mu]t}\langle\Psi(0)|\Psi(t)\rangle\right],$$
(3)

where we have used the initial condition $|\Psi(0)\rangle = c_{i\sigma}^\dagger|\Psi_0^N\rangle$ and $0^+$ is a positive infinitesimal quantity and the calculated object is the Green's function $\langle\Psi(0)|\Psi(t)\rangle$. In a similar way the photoemission spectrum can be calculated. These formulas are discussed in detail in the appendix [17].

*Methods.* To compute $|\Psi(t)\rangle$ accurately for long propagation times, we have adapted the Full Configuration Interaction Quantum Monte Carlo (FCIQMC) method [18–21]. This method was originally designed to stochastically project the wave function, expressed in a full Slater determinant basis $\{|D_i\rangle\}$, towards the ground state. The ground state algorithm uses a stochastic representation of the full CI wave function $\Psi = \sum_i C_i |D_i\rangle$ using signed walkers, $C_i$, together with the repeated stochastic application of a short-time propagator $\hat{P}(\Delta\tau) = \mathbb{1} - \Delta\tau\hat{H}$ to the population of walkers, followed by walker annihilation at the end of each iteration. More details are given in the appendix [17].

Generalizing to the time dependent problem, the wave function $\Psi(t) = \sum_i C_i(t) |D_i\rangle$ is represented by a collection of complex walkers, the time evolution of which is realized through the successive application of a *second-order* propagator:

$$\hat{U}_2(\Delta t) = \mathbb{1} - \mathrm{i}\Delta t\hat{H} - \frac{1}{2}\left(\Delta t\right)^2\hat{H}^2.$$
(4)

where $\Delta t$ is a small time-step. Thus $\Psi(t + \Delta t) = \hat{U}_2(\Delta t)\Psi(t)$. This approach preserves the norm of the wave function to order $\mathcal{O}(\Delta t^4)$ per step and $\mathcal{O}(\Delta t^3)$ in total, which is found to be sufficient to allow for stable propagation for a long time, without significant norm-conservation errors. In contrast, propagation using a first-order propagator only leads to norm-conservation of order $\Delta t$, which leads to a severe violation of unitarity over relevant time-scales. The time evolution is implemented using a second-order Runge-Kutta algorithm. Numerical examples are provided in the appendix [17].

Although this method remains unitary to a good approximation, stochastic errors lead to a growth of the norm over time (see appendix [17]), which becomes unmanageable for large Hilbert spaces. We therefore allow the time step $\Delta t$ to acquire a phase $\alpha$

$$\Delta t \mapsto \mathrm{e}^{-\mathrm{i}\alpha}\Delta t,$$
(5)

thereby introducing a damping in the propagator. The phase is varied dynamically to keep the number of walkers approximately constant. A small number of walkers requires a large $\alpha$, and increasing the number of walkers reduces $\alpha$. The pure real-time propagation ($\alpha = 0$) is achieved in the large walker limit. Since $\alpha \neq 0$ results in complex-time Green's functions, we have generalized the (imaginary time) MaxEnt method [15, 16] to compute $A(\omega)$ (see appendix [17]). The analytic continuation is more accurate for small $\alpha$, and robustness of the calculated spectra can be checked by comparing results for different numbers of walkers. To obtain the statistics needed for the MaxEnt method, we run several independent calculations.

Compared with the finite temperature Matsubara (imaginary time) formalism, this leads to three advantages. i) The MaxEnt method gives a more detailed spectrum, since the time path is rather close to the real axis, rather than along the imaginary axis. ii) In each spectral calculation we shift $\mu$ so that the peak closest to $\mu$ is located at $\mu$. Since MaxEnt is most accurate close to $\mu$, this improves the accuracy. iii) For a given $\mathbf{k}$, the weight of the PE and IPE spectra may be very different. By performing the PE and IPE calculations separately, we obtain a comparable relative standard deviation in both cases, in contrast to the Matsubara formulation. These aspects are discussed in the appendix [17] and illustrated in Fig. 1c below.

*Application to the Hubbard model.* As a first example, we consider the fermionic Hubbard model [8]. It is defined by the Hamiltonian $H = -t\sum_{\langle i,j\rangle\sigma} c_{i\sigma}^\dagger c_{j\sigma} + U\sum_i n_{i\uparrow}n_{i\downarrow}$. We consider a two-dimensional square-lattice with periodic boundary conditions.

We apply the method to an 18-site cluster (18A in Betts' notation[23]) at half-filling, which is among the largest Hubbard systems whose Green's function can be calculated numerically exactly using Lanczos recursion [13, 24] (with a Hilbert space consisting of $\sim 2.4 \times 10^9$ determinants). To compute the Green's function, we first converge the ground state using imaginary-time FCIQMC, and then perform a complex time calculation with a $\mathbf{k} = (0,0)$ electron removed from the ground state. A plane waves basis set is used here.

Three calculations are shown in Fig. 1 for $U/t = 2$, employing 70000, $1.6 \times 10^6$ and $17 \times 10^6$ walkers, with the corresponding time contours in the complex plane shown in the inset. Even though the resulting spectrum for the smallest walker number is qualitatively correct, it is broadened and shifted versus the Lanczos spectrum. Increasing the walker number to $1.6 \times 10^6$ gives less se-
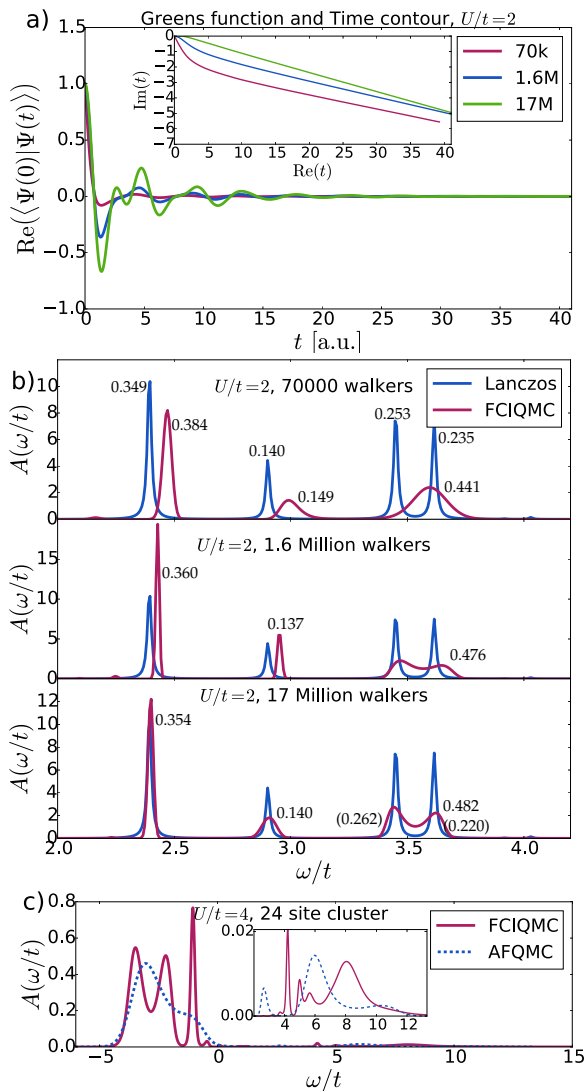
FIG. 1. (a) Time evolution of Re $\langle\Psi(0)|\Psi(t)\rangle$ and contour in complex time and (b) corresponding photoemission spectra (for $\mu = 0$) for the time-evolution using 70000, $1.6 \times 10^6$ and $1.7 \times 10^7$ walkers for the 18-site Hubbard model at $U/t = 2$, $k = (0,0)$ and half-filling. All calculations start from the same initial state with 350000 walkers, and three different time contours were used leading to 70000, $1.6 \times 10^6$ and $1.7 \times 10^7$ walkers for longer times. The utilized time-step is $10^{-3}$. Both the Lanczos and FCIQMC spectra were convoluted with a Lorentzian of full width at half maximum (FWHM) of 0.02 to simplify visual comparison of the FCIQMC spectrum to the discrete eigenvalues obtained in the Lanczos method. The integrated weights of the peaks of the FCIQMC spectra are indicated and agree well with the weights of the discrete Lanczos spectrum, which are given in the first graph of b). The bracketed numbers indicate the weights of not fully resolved peaks. (c) Photoemission and inverse photoemission spectra for a 24-site cluster with lattice vectors (3,3) and (-5,3) with 22 electrons at $U/t = 4$ for $k = (0,0)$ obtained using $\sim 1.5 \times 10^8$ and $\sim 3 \times 10^7$ walkers respectively. The inverse photoemission part carries very low weight and is also shown in the inset. For comparison, the same spectrum computed by means of the Hirsch-Fye[22] auxiliary-field quantum Monte Carlo (AFQMC) is displayed.

vere damping. The peaks are still slightly displaced compared to the exact result. For $17 \times 10^6$ walkers, $\alpha$ is small ($\approx 0.12$) and the spectrum is fully resolved with the peaks in their correct positions. The agreement in the weight distribution also serves as an indicator of the impact of the walker number. The memory used here is 270 Mb per processor. This already involves significant performance-memory tradeoffs, such that a single replica of this calculation can be run with less than 800 Mb total memory, more than a factor of 70 smaller than for the exact diagonalization.

Fig. 1c) shows the PE and IPE spectra for a 24-site cluster with 22 electrons (24E in Betts' notation[23]). This illustrates that calculations can be performed for doped systems and for much larger Hilbert spaces ($\sim 6 \times 10^{12}$) than exact diagonalization. For the IPE spectrum, the main quasi-particle peak and the main satellite peak at higher energies are well-resolved. This spectrum is highly difficult to compute since the initial wave func-

tion is highly multiconfigurational, as it is obtained by eliminating the Hartree-Fock determinant keeping a very high number of leading determinants with similar weight. For the PE spectrum, both the main quasi-particle peak as well as two satellite peaks can be clearly identified. As a comparison, we show results using the Hirsch-Fye (HF) method,[22] based on the Matsubara formalism for $T = 0.2t$. The HF PE spectrum is consistent with the FCIQMC spectrum, but the peaks are not resolved. This is due factors i) and ii) above (performing analytical continuation from imaginary times and not being able to shift the peak at -2.5t to 0). The weight of the IPE spectrum is only 0.035 and the relative standard deviation about a factor of 25 larger for the part of the Green's function relevant for IPE than for the PE relevant part [iii) above].

*Application to ab-initio systems.* We employ the scheme for *ab-initio* systems, namely the carbon atom and the carbon dimer at equilibrium distance. Here, the
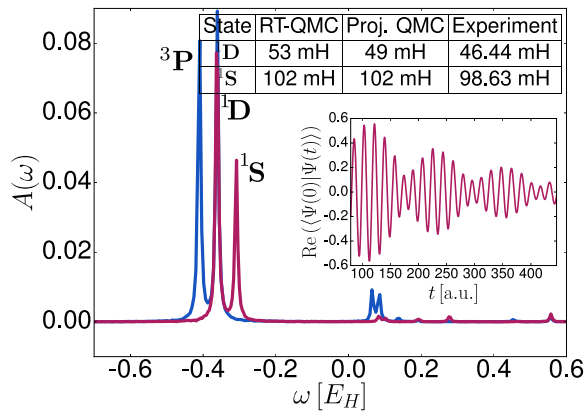
FIG. 2. Atomic multiplet of the carbon atom, obtained from two distinct initial states created by adding a 2p electron to the cation ground state. One of the states is prepared as a singlet (red), the second state (blue) is a mixture of singlet and triplet but with $L_z \neq 0$. The time-evolution is carried out for 1600 a.u. of time and the zero of the frequency axis corresponds to $-37.3706\,\text{H}$ which is the ground state energy of the cation computed using the projective FCIQMC algorithm. The VTZ basis is used in this example. The experimental values are according to [25]. The frequency resolution is $3.9\,\text{mH}$. The inset shows a portion of the computed Green's function in real time.
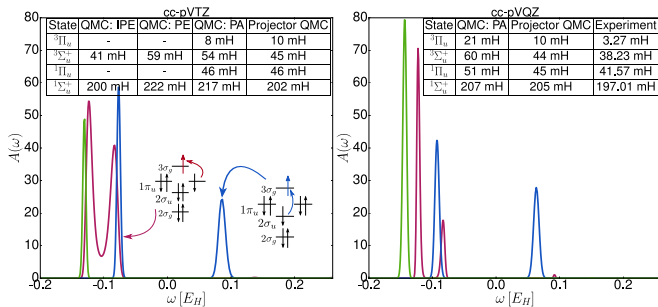


FIG. 3. Photoabsorption spectra for the carbon dimer for a single excitation from the $2\sigma_u$ to the $3\sigma_g$ (blue) and from the $1\pi_u$ to the $3\sigma_g$ (red) orbital using V$X$Z basis sets. Also shown is spectral decomposition of the FCIQMC ground state (green) as a reference . The spectra are not normalized for better display. For the VTZ basis set, we also computed $\Sigma_u$-photoemission (PE) and inverse photoemission (IPE) spectra for the $\text{C}_2^-$ and $\text{C}_2^+$ respectively. All energies and spectra are obtained with MaxEnt analytic continuation from 44-48 independent calculations. The experimental values are taken from[26], these are also used to attribute singlet and triplet states and the $\pm$-symmetry of the $\Sigma$-states. The zero of the frequency axis is set to $-75.649\,\text{H}$. The time-step used is $\Delta t = 10^{-3}$ for the VTZ basis set, and $\Delta t = 10^{-3}$ (green) and $\Delta t = 5 \times 10^{-4}$ (red,blue) for the VQZ basis set.

Hamiltonian is the molecular Hamiltonian in the Born-Oppenheimer approximation

$$H = \sum_{p,q,\sigma} h_q^p c_{p\sigma}^\dagger c_{q\sigma} + \sum_{p,q,r,s,\sigma\tau} V_{qp}^{rs} c_{r\sigma}^\dagger c_{s\tau}^\dagger c_{p\tau} c_{q\sigma}\,, \qquad (6)$$

where $h_q^p$ contains the one-body integrals of the Schrödinger Hamiltonian, and $V_{pq}^{rs}$ the two-body Coulomb integrals of the electron-electron interaction. We used the cc-pV$X$Z basis sets with $X$=T,Q (referred to as V$X$Z in the following), containing 28 and 54 functions per atom respectively, in the frozen-core approximation. The required Hamiltonian integrals were computed over restricted Hartree-Fock orbitals using MOLPRO [29].

For the carbon atom, we show the multiplet structure of the ground state in Fig. 2, obtained over a trajectory of 1600 a.u. of time.

Due to the small system size, we performed the propagation in pure real-time, with a time-step of $\Delta t = 5 \times 10^{-3}$. A small constant damping with a decay constant of $3\,\text{mH}$ is applied that has negligible influence on the spectral function, but reduces the growth of walkers and allows for longer propagation times. The cation ground state energy from the ground state computation for the preparation of the initial state is $E_0^{N-1} = -37.3706\,\text{H}$, which gives an ionization energy of $420\,\text{mH}$, agreeing reasonably well with the experimental finding of $413.8\,\text{mH}$ [25]. The inset of Fig. 2 shows the oscillations of the overlap $\langle\Psi(0)\,|\,\Psi(t)\rangle$ and corresponding spectra. The resulting excitation energies agree fairly well with experiment.

Next, we consider spectral functions of a prototypical strongly correlated molecule, the carbon dimer at equilibrium distance. To target specific states, we simulate photoabsorption (PA) spectroscopy. To do so, the initial $^1\Sigma_g^+$ state is prepared by performing a ground state calculation on the neutral carbon dimer using FCIQMC, and then applying the single excitation operator $c_i^\dagger c_j$ on the resulting walker population. Specifically, we consider the excitations from $1\pi_u$ to the $3\sigma_g$ and the excitation from $2\sigma_u$ to $3\sigma_g$. The former couple to $\Pi_u$ states, whilst the latter couple to $\Sigma_u^+$ states. Since the excitations generate open-shell determinants, the resulting spectra couple to both singlet and triplet states.

The resulting spectra for the two basis sets are shown in Fig. 3, we additionally compare to projector QMC values computed using the excited-state i-FCIQMC method [27] and using the ground state energies calculated in [28] as references. The involved Hilbert spaces contain respectively $10^{10}, 10^{12}$ Slater determinants. Sharply resolved peaks which correspond to $^3\Pi_u, ^3\Sigma_u^+, ^1\Pi_u, ^1\Sigma_u^+$ could be identified. We also performed photoemission and inverse photoemission calculations for the $\text{C}_2^-$ and $\text{C}_2^+$ respectively, the resulting energies for the excited states of the neutral $\text{C}_2$ are listed in Fig. 3. We find that the inverse photoemission spectra feature the lowest stochastic error while the photoemission results have a higher error. A rotation of time in the complex plane by an angle of $\alpha$ in the range $[0.1, 0.2]$ is applied. The dependence of the spectra on the basis set is in line with the known basis-set dependence of relative energies in molecular systems, for example ionisation energies and electron affinities from FCIQMC quantum chemical studies [19, 30, 31]. The

vertical transition energies obtained here are larger than the experimentally observed values. A previous analysis by Holmes et al. [32] of the excited state potential energy curves shows a significant effect of bond-length variation for the states considered here, indicating the likely non-vertical character of the experimental transitions.

*Conclusions.* We have presented an efficient method for solving the time-dependent Schrödinger equation. We generalize a full configuration interaction Quantum Monte Carlo method to calculations for complex times close to the real axis. We then develop a maximum entropy method for analytic continuation from complex times to real frequency. The method can be used to calculate electron spectra. The imaginary component of time strongly limits the numerical effort without a strong negative impact on the analytic continuation. We demonstrated that spectra of the Hubbard model can be obtained in good agreement with exact Lanczos calculations. We then applied the method to *ab initio* systems, the C atom and the $C_2$ molecule, and obtained good agreement with experiment for excitation energies. The method can be used as cluster solver in embedding schemes for solids. It can also be used to study small systems in strong external fields without any assumptions about linear response.

---

* k.guther@fkf.mpg.de
† w.dobrautz@fkf.mpg.de
‡ o.gunnarsson@fkf.mpg.de
§ a.alavi@fkf.mpg.de

[1] L. Hedin and S. Lundqvist, Solid State Physics **23**, 1 (1970).
[2] D. W. Turner, Philosophical Transactions of the Royal Society of London A: Mathematical, Physical and Engineering Sciences **268**, 7 (1970).
[3] F. J. Himpsel and T. Fauster, Journal of Vacuum Science & Technology A: Vacuum, Surfaces, and Films **2**, 815 (1984).
[4] J. J. Pireaux, S. Svensson, E. Basilier, P.-A. Malmqvist, U. Gelius, R. Caudano, and K. Siegbahn, Phys. Rev. A **14**, 2133 (1976).
[5] P. Mills and J. L. Sullivan, Journal of Physics D: Applied Physics **16**, 723 (1983).
[6] A. Polkovnikov, K. Sengupta, A. Silva, and M. Vengalattore, Rev. Mod. Phys. **83**, 863 (2011).
[7] G. Onida, L. Reining, and A. Rubio, Rev. Mod. Phys. **74**, 601 (2002).
[8] J. Hubbard, Proc. Roy. Soc. London A **276**, 238 (1963).
[9] P. W. Anderson, Phys. Rev. **124**, 41 (1961).
[10] T. Maier, M. Jarrell, T. Pruschke, and M. H. Hettler, Rev. Mod. Phys. **77**, 1027 (2005).
[11] E. Gull, A. J. Millis, A. I. Lichtenstein, A. N. Rubtsov, M. Troyer, and P. Werner, Rev. Mod. Phys. **83**, 349 (2011).
[12] J. Crank and P. Nicolson, Proc. Camb. Phil. Soc. **43**, 50 (1947).
[13] B. N. Parlett, *The symmetric eigenvalue problem* (Prentice, Englewood, 1980) p. 257.
[14] T. Park and J. Light, J. Chem. Phys. **85**, 5870 (1986).
[15] R. N. Silver, D. S. Sivia, and J. E. Gubernatis, Phys. Rev. B **41**, 2380 (1990).
[16] M. Jarrell and J. Gubernatis, Phys. Rep. **269**, 133 (1996).
[17] See appendix for a summary of the FCIQMC method, a more detailed discussion of the calculation of Green's functions and optical absorption spectra, details of the time-evolution algorithm regarding the complex time contour as well as the usage of a second order Runge-Kutta scheme, and a discussion of the MaxEnt methodology. The appendix additionally includes references [33–39].
[18] G. H. Booth, A. J. W. Thom, and A. Alavi, The Journal of Chemical Physics **131**, 054106 (2009).
[19] G. H. Booth and A. Alavi, The Journal of Chemical Physics **132**, 174104 (2010).
[20] D. Cleland, G. H. Booth, and A. Alavi, The Journal of Chemical Physics **132**, 041103 (2010).
[21] G. H. Booth, A. Gruneis, G. Kresse, and A. Alavi, Nature **493**, 365 (2012).
[22] J. E. Hirsch and R. M. Fye, Phys. Rev. Lett. **56**, 2521 (1986).
[23] D. D. Betts, H. Q. Lin, and J. S. Flynn, Canadian Journal of Physics **77**, 353 (1999), https://doi.org/10.1139/p99-041.
[24] O. Gunnarsson and K. Schönhammer, *Handbook on the physics and chemistry of rare earths*, edited by K. A. Gschneider Jr., L. Eyring and S. Hüfner **10**, 103 (1987).
[25] V. Kaufman and J. F. Ward, J. Opt. Soc. Am. **56**, 1591 (1966).
[26] M. Martin, J. Photochem. Photobiol. A: Chem **66**, 263 (1992).
[27] N. S. Blunt, S. D. Smart, G. H. Booth, and A. Alavi, The Journal of Chemical Physics **143**, 134117 (2015).
[28] D. Cleland, G. H. Booth, C. Overy, and A. Alavi, Journal of Chemical Theory and Computation **8**, 4138 (2012), pMID: 26605580.
[29] H.-J. Werner, P. J. Knowles, G. Knizia, F. R. Manby, and M. Schütz, WIREs Comput Mol Sci **2**, 242 (2012).
[30] D. M. Cleland, G. H. Booth, and A. Alavi, The Journal of Chemical Physics **134**, 024112 (2011).
[31] G. H. Booth, D. Cleland, A. J. W. Thom, and A. Alavi, J. Chem. Phys. **135**, 084104 (2011).
[32] A. A. Holmes, C. J. Umrigar, and S. Sharma, The Journal of Chemical Physics **147**, 164111 (2017), https://doi.org/10.1063/1.4998614.
[33] C. Daday, S. D. Smart, G. H. Booth, A. Alavi, and C. Filippi, J. Chem. Theory Comput. **8**, 4441 (2012).
[34] J. J. Shepherd, G. H. Booth, A. Grüneis, and A. Alavi, Phys. Rev. B **85**, 081103 (2012).
[35] F. R. Petruzielo, A. A. Holmes, H. J. Changlani, M. P. Nightingale, and C. J. Umrigar, Phys. Rev. Lett. **109**, 230201 (2012).
[36] N. S. Blunt, S. D. Smart, J. A. F. Kersten, J. S. Spencer, G. H. Booth, and A. Alavi, The Journal of Chemical Physics **142**, 184107 (2015).
[37] C. Overy, G. H. Booth, N. S. Blunt, J. J. Shepherd, D. Cleland, and A. Alavi, The Journal of Chemical Physics **141**, 244117 (2014).
[38] L. Verlet, Phys. Rev. **159**, 98 (1967).
[39] O. Gunnarsson, M. W. Haverkort, and G. Sangiovanni, Phys. Rev. B **81**, 155107 (2010).

## APPENDIX

## Recap of the FCIQMC method

The FCIQMC method [18–20] is a projector quantum Monte Carlo method based on the imaginary-time Schrödinger equation. It has the stationary form

$$\frac{\partial}{\partial \tau}|\Psi\rangle = -(\hat{H} - E_0)|\Psi\rangle = 0, \qquad (7)$$

with formal solution:

$$|\Psi(\tau)\rangle = e^{-\tau(\hat{H} - E_0)}|\Psi(0)\rangle \qquad (8)$$

which converges (up to a normalization constant) to the ground state $|\Psi_0\rangle$ of $\hat{H}$ in the large $\tau$ limit. We define a first-order propagator $\hat{P}$ as

$$\hat{P} = \mathbb{1} - \Delta\tau(\hat{H} - S\mathbb{1}), \qquad (9)$$

where $\Delta\tau$ is a time-step and $S$ an energy shift to control the walker number. If $\hat{H}$ has a finite spectral width $W$, repeated application leads to the ground-state

$$|\Psi(n\Delta\tau)\rangle = \hat{P}^n|\Psi(0)\rangle \qquad (10)$$
$$\lim_{n\to\infty}|\Psi(n\Delta\tau)\rangle \propto |\Psi_0\rangle,$$

without a time-step error, if $\Delta\tau$ is smaller than $\frac{2}{W}$. $|\Psi(\tau)\rangle$ is expressed as a linear combination of a complete set of basis states $|D_i\rangle$

$$|\Psi(\tau)\rangle = \sum_i C_i(\tau)|D_i\rangle \qquad (11)$$

In FCIQMC, the coefficients $C_i$ are replaced by an ensemble of positive and negative *walkers*:

$$C_i \propto N_i = \sum_w^{N_w} s_w \delta(i - i_w) \qquad (12)$$

where $s_w = \pm 1$ is the sign of the walker $w$, residing on Slater determinant $i_w$. $N_w$ is the number of walkers. The walkers evolve according to stochastic rules

- A spawning step: a given walker, on $|D_i\rangle$, randomly selects another connected determinant, $|D_j\rangle$ with probability $p_{gen}(j|i)$. It then attempts to spawn a new walker on $|D_j\rangle$ with probability $p_s = -\Delta\tau H_{ij}/p_{gen}(j|i)$.

- A death/cloning step: A walker on $D_i$ attempts to die with probability $p_d = \Delta\tau(H_{ii} - S)$.

In a following step, walkers with opposite signs cancel each other, which is essential for addressing the sign-problem. In the initiator version of the algorithm [20, 28, 30] the spawning is restricted. If the target determinant is not occupied by another walker, the spawning is aborted if $|N_i| \leq n_a$, where $n_a$ is the initiator parameter. This condition is crucial for obtaining a smooth convergence without too many walkers.

For the calculation of reduced density matrices (RDM), we use the replica method [37], in which two independent simulations of walkers are propagated and elements of the RDMs are being calculated by taking products involving the two replicas.

The main advantage of the FCIQMC algorithm compared to conventional exact diagonalization is that the number of walkers needed for convergence is much smaller than the dimension of the Hilbert space, thereby requiring drastically less memory. Using this technique, molecular and condensed-matter systems involving Hilbert spaces of over $10^{20}$ Slater determinants have been computed [33, 34].

## Norm conservation

Compared to the pure imaginary time evolution, the complex exponential in the real-time formulation does not cause an exponential decay of contributions from excited states, but instead gives a complex phase to the walkers, which requires the use of both real and imaginary walkers for each determinant. Here, real and imaginary populations are only coupled via the stochastic application of the first-order expanded propagator

$$\hat{U}_1(t) = 1 - i\hat{H}t. \qquad (13)$$

The annihilation step is performed separately for each of the populations.

The direct use of $\hat{U}_1$ in the time propagation leads to an exponentially increasing wave function, and therefore severely violates norm-conservation of unitary dynamics. This can be seen by considering the time evolution of a wave function $\Psi = \Psi_0$ that is already an eigenstate of the Hamiltonian with energy $E$. The exact solution is

$$|\Psi(t)\rangle = e^{-iEt}|\Psi_0\rangle \qquad (14)$$

According to the first-order propagator, after $n$ application of $\hat{U}_1$ we obtain:

$$|\Psi(t_n)\rangle = (1 - iE\Delta t)^n|\Psi_0\rangle, \qquad (15)$$

with $t_n = n\Delta t$, we obtain:

$$\ln\frac{\Psi(t_n)}{\Psi_0} = n\ln(1 - iE\Delta t) \approx -iEt_n + \frac{E^2 t_n \Delta t}{2} \qquad (16)$$

so that:

$$|\Psi(t_n)\rangle = e^{-iEt_n}e^{E^2 t_n \Delta t/2}|\Psi_0\rangle \qquad (17)$$

which is exponentially growing in time, with an exponent $\mathcal{O}(\Delta t)$. This is a direct consequence of working with real

time, which introduces a growing exponential factor in Eq. (17).

This problem can be greatly suppressed using a second-order short-time propagator. Defining:

$$\hat{U}_2(\Delta t) = \mathbb{1} - \mathrm{i}\Delta t \hat{H} - \frac{1}{2}(\Delta t)^2 H^2 \qquad (18)$$

The time evolution is implemented using a second-order Runge-Kutta algorithm, which decomposes $\hat{U}_2$ into two steps:

$$\hat{U}_2(\Delta t) = \mathbb{1} + \left(\hat{U}_1(\Delta t) - \mathbb{1}\right)\hat{U}_1\left(\frac{\Delta t}{2}\right). \qquad (19)$$

The second order propagator is applied by first applying $\hat{U}_1\left(\frac{\Delta t}{2}\right)$ to the wavefunction, followed by applying $\left(\hat{U}_1(\Delta t) - \mathbb{1}\right)$ to the result and finally adding the resulting wavefunction to the original one. In this way, $\hat{H}^2$ is not explicitly applied, which is highly advantageous for the efficiency of the method.

We now have after $n$ repetitions of $\hat{U}_2$:

$$|\Psi(t_n)\rangle = [1 - iE\Delta t - \frac{(E\Delta t)^2}{2}]^n|\Psi_0\rangle \qquad (20)$$

resulting in:

$$\ln\frac{\Psi(t_n)}{\Psi_0} = n\ln[1 - \mathrm{i}E\Delta t - \frac{(E\Delta t)^2}{2}] \qquad (21)$$

$$\approx -\mathrm{i}Et_n - \mathrm{i}\frac{E^3 t_n(\Delta t)^2}{6} + \frac{E^4 t_n(\Delta t)^3}{8}$$

$$|\Psi(t_n)\rangle = e^{-\mathrm{i}Et_n}e^{-\mathrm{i}E^3 t_n(\Delta t)^2/6}e^{E^4 t_n(\Delta)^3/8}|\Psi_0\rangle$$

i.e. in this formulation the norm-violating factor grows only as $\mathcal{O}(\Delta t^3)$. It is possible to reduce further the scaling of norm-violation by employing a 4-th order propagator, but we found that improvements are typically masked by much larger stochastic errors.

Fig. 4 compares the first and second order expansions in the Rung-Kutta method. The figure illustrates how the number of walkers and the norm rapidly increase in the first order expansion. The first order overlap $\langle\Psi_i^\pm(0)|\Psi_i^\pm(t)\rangle$ is substantially more accurate than the norm, but still not satisfactory.

Fig. 5 (right part) compares deterministic[36? ] and stochastic calculations of time evolutions of the norm $\langle\Psi(t)|\Psi(t)\rangle$ to second order. The deterministic calculation only contains the errors of the second order Runge-Kutta, and it is very accurate over this time scale. The stochastic calculation introduces substantial errors in the norm, e.g., due to excitations to high-lying states. In the overlap $\langle\Psi_j^\pm(0)|\Psi_i^\pm(t)\rangle$ these stochastic errors tend to cancel (see left part of Fig. 5) for two reasons. Many of the stochastically excited states have little or no weight in the initial state and therefore give little or no contribution to the overlap. Furthermore, the stochastic errors
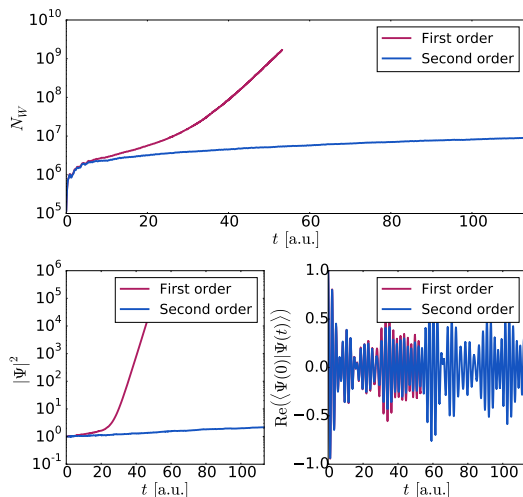


FIG. 4. Number of walkers $N_W$, norm of the wave function, and Green's function for the 10-site Hubbard model, $k = (0,0)$ and $U/t = 1$, using the stochastic algorithm and the first and second order Runge-Kutta methods.

due to the time evolution enter linearly in $\langle\Psi_j^\pm(0)|\Psi_i^\pm(t)\rangle$ and therefore tend to cancel. This is crucial for the accuracy of the method. We could alternatively have calculated $\langle\Psi_j^\pm(t/2)|\Psi_i^\pm(t/2)\rangle$, but in this case the stochastic errors are much larger, since the the two arguments above do not apply.

Even though a symplectic integrator such as the Verlet method [38] could in principle yield smaller discretization errors, we find that stochastic errors play a much larger role, making it unfeasible compared to the Runge-Kutta integrator.

### Computation of Green's functions and optical absorption

Here, we provide some more details about the calculation of the Green's function.

We assume that the ground-state $|\Psi_0^N\rangle$ for $N$ electrons has been calculated. We then want to calculate the Green's function

$$G_{ij}(t) = -i\langle\Psi_0^N|T\{c_i(t)c_j^\dagger\}|\Psi_0^N\rangle, \qquad (22)$$

where $T$ is the time-ordering operator, $c_i$ is the annihilation operator for an electron with quantum numbers $i$ (including spin) and $c_i(t) = \exp(i\hat{H}t)c_i\exp(-i\hat{H}t)$. For $t < 0$ ($t > 0$) this corresponds to (inverse) photoemission. For photoemission we make a variable substitution $t \to -t$. Then both photoemission and inverse photoemission correspond to positive time propagation, but there is now an extra minus sign in the Schrödinger equation for photoemission. We then consider the initial state

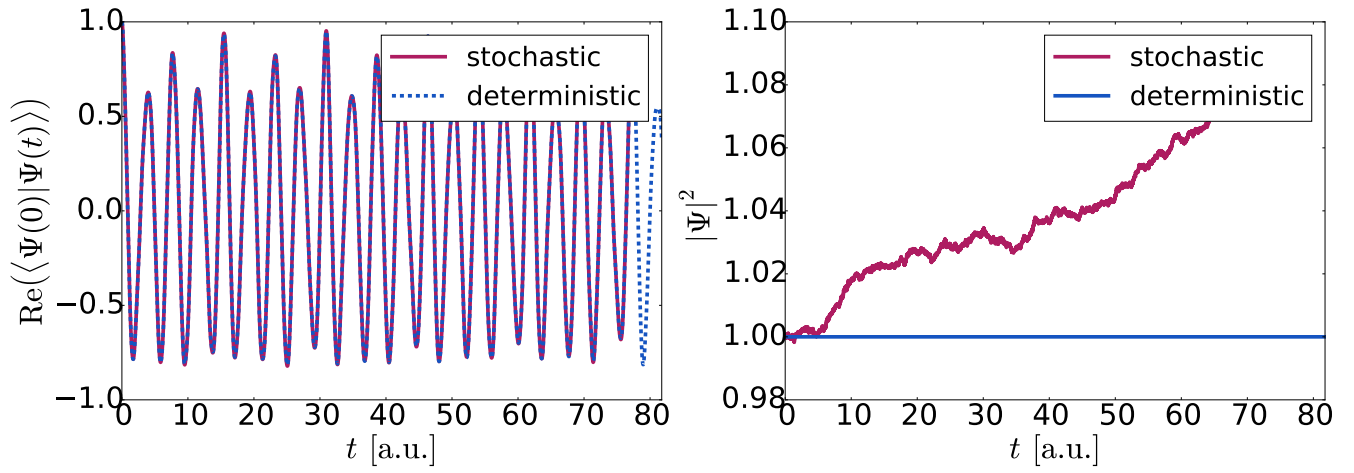$$|\Psi_i^\pm(0)\rangle = c_i^\pm|\Psi_0^N\rangle, \qquad (23)$$

FIG. 5. Green's function (left) and norm (right) of the wave function over time using the second-order algorithm for the two-dimensional 10-site Hubbard model, $k = (0,0)$ and $U/t = 1$. Both were calculated using both stochastic and deterministic algorithms.

where lower (upper) sign indicates (inverse) photoemission and $c_i^+ = c_i^\dagger$ and $c_i^- = c_i$. We solve the Schrödinger equation

$$i\frac{d}{dt}|\Psi_i^\pm(t)\rangle = \pm[e^{\mp i\alpha(t)}(\hat{H} - E_0^N \mp \mu)]|\Psi_i^\pm(t)\rangle, \quad (24)$$

Here $\alpha(t)$ defines the path through the complex time plane. $\alpha(t) \equiv 0$ $(\pi/2)$ corresponds to integration along the real (imaginary) time axis. The formal solution can be written as

$$|\Psi_i^\pm(t)\rangle \quad (25)$$
$$= \exp[\mp i \int_0^t dt' e^{\mp i\alpha(t')}(\hat{H} - E_0^N \mp \mu)]|\Psi_i^\pm(0)\rangle$$

We take the overlap to the state $\langle\Psi_j^\pm(0)|$ and expand this in a complete set of states $|\Psi_n^{N\pm1}\rangle$.

$$\langle\Psi_j^\pm(0)|\Psi_i^\pm(t)\rangle \quad (26)$$
$$= \sum_n \langle\Psi_0^N|c_j^\mp|\Psi_n^{N\pm1}\rangle\langle\Psi_n^{N\pm1}|c_i^\pm|\Psi_0^N\rangle$$
$$\times\exp\{\mp i \int_0^t dt'\exp[\mp i\alpha(t')][E_n^{N\pm1} - E_0^N \mp \mu]\}$$
$$= \int d\omega A_{ji}^\pm(\omega)\exp\{-i \int_0^t dt'\exp[\mp i\alpha(t')]\omega\}$$

Here we have introduced the spectral functions

$$A_{ji}^\pm = \sum_n \langle\Psi_0^N|c_j^\mp|\Psi_n^{N\pm1}\rangle \quad (27)$$
$$\times\langle\Psi_n^{N\pm1}|c_i^\pm|\Psi_0^N\rangle\delta[\omega \mp E_n^{N\pm1} \pm E_0^N + \mu]$$

We finally introduce the spectral function

$$A_{ij}(\omega) = A_{ij}^+(\omega) + A_{ij}^-(\omega), \quad (28)$$

where we have used conventions that negative (positive) frequencies correspond to (inverse) photoemission. Large (small) values of $|\omega|$ correspond to excited states with large (small) excitation energy. In a similar way we can calculate optical conductivity, by applying a current operator to the $N$-particle state and propagating this in time.

The targeted spectral function then dictates the structure of the initial wavefunction, and thereby also the level of correlation present in the initial state. As $\Psi_0^N$ is taken from a previous FCIQMC calculation, the initial state is obtained from a stochastic sample of the true ground-state. Therefore, multiple independent samples of $\Psi_0^N$ are taken, and the Green's function is computed from the overlap of the initial state of one sample with the time-evolution of another, since a Green's function from only a single sample is quadratic in the initial state and is hence potentially biased. We find that such a bias is problematic only for the most correlated initial states, like the inverse photoemission for the 24-site Hubbard model as in Fig. 6, but using a Green's function obtained from a single sample should be avoided nevertheless.

**Complex time contour**

We use a time-dependent angle $\alpha(t)$, which is adjusted so that the number of walkers do not appreciably exceed a preset value. This is done in a similar way as the walker number control in the projective algorithm. We prescribe an initial value $\alpha(t = 0) = \alpha_0$, typically $\alpha_0 = 0$. Once the walker number exceeds a threshold value $N_{\text{target}}$, we
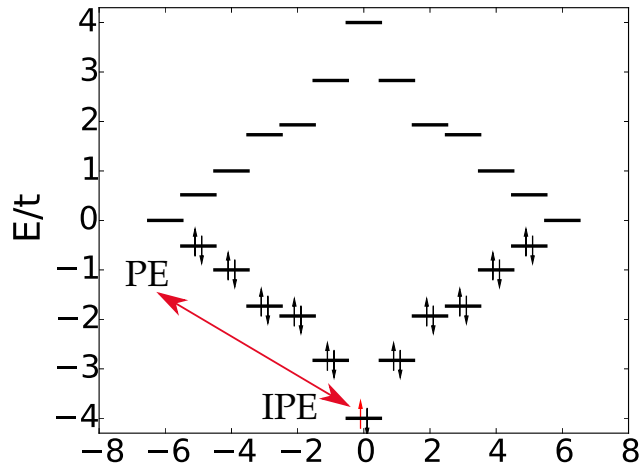
FIG. 6. Energy levels of the non-interacting 24-site Hubbard model with lattice vectors $(3,3)$ and $(-5,3)$. The (inverse) photoemission spectrum for $k = (0,0)$ is obtained by removing (adding) the electron marked in red. While removing an electron with $k = (0,0)$ keeps the determinant with highest weight and therefore creates an initial state with a unique high-weight leading determinant, this is not the case for the inverse photoemission. As $k = (0,0)$ is doubly occupied in the reference determinant of the ground state, the latter does not appear in the initial state and we start from a enormously correlated state with a high number of determinants with comparable weight.

start to adjust $\alpha$ every $B$ steps as

$$\alpha(t + B\Delta t) = \alpha(t) + \xi \arctan\left(\frac{N_W(t + B\Delta t)}{N_W(t)} - 1\right). \tag{29}$$

Here, $N_w(t)$ is the number of walkers at time $t$ and $\xi \sim 0.1 - 1.0$ is a damping parameter. Using this heuristic approach, the value of alpha is iteratively updated to counter changes in the walker number. We use the arctan function to map changes in walker number to changes in an angle, but for sufficiently small $B \approx 10$, we do not expect the exact choice of the function used for this mapping to have an impact. Using this technique, the value of $\alpha$ is increased during the time evolution as the walker number increases, which in turn damps the walker number growth, eventually leading to an equilibration of both the value of $\alpha$ and the number of walkers. However, depending on the chosen parameters $\xi$ and $B$, even in equilibrium, the value of $\alpha$ can be subject to rapid fluctuations around the average value due to short-time fluctuations in the number of walkers. This has no notable impact on the contour, however. The equilibrium value of $\alpha$ is then typically $\sim 0.05 - 0.25$ for the studied systems, except for the 24-site Hubbard model with an equilibrium value of $\alpha \sim 0.45$. Increasing the walker threshold value $N_{\text{target}}$ tends to decrease $\alpha$.

### *Walker number dependence*

The walker number impacts the time-evolution in two ways. The first is the influence on the adaptation of $\alpha$, as increasing the walker number for a fixed initial num-

ber of walkers lowers the required values of $\alpha$ for a stable calculation with a constant walker number. The control mechanisms for adjusting the walker number here are setting the initial value $\alpha_0$ and/or a minimum walker number which has to be reached before the value of $\alpha$ is changed. In particular only adjusting $\alpha$ once a given number of walkers is reached allows for targeting specific walker numbers, similar to the variable shift mode in the projected algorithm, although the walker number equilibration is typically slower. The values $\alpha$ obtains in this procedure decrease as the targeted walker number is increased, while increasing $\alpha_0$ unsurprisingly decreases the number of walkers used.

The second effect is a bias in the Green's function itself as shown in figure 7.

### **Chemical potential shift**

Typically we are particularly interested in the spectrum relatively close to the chemical potential (within several eV). We can emphasize these states by using the flexibility of the present method. Thus we study the spectra for each $\mathbf{k}$ at a time and photoemission and inverse photoemission separately. We then have the freedom to choose the chemical potential as $E_0^N - E_0^{N-1}(\mathbf{k}) \leq \mu \leq E_0^{N+1}(\mathbf{k}) - E_0^N$ in the spectral calculation, where $E_0^M(\mathbf{k})$ is the lowest $M$-electron state with the wave vector $\mathbf{k}$. Lowering (increasing) $\mu$ for (inverse) photoemission leads to a slower decay of the Green's function for a given $\alpha(t)$. The shift increases the weight of all states. To keep the number of walkers fixed, $\alpha(t)$ is then increased. This
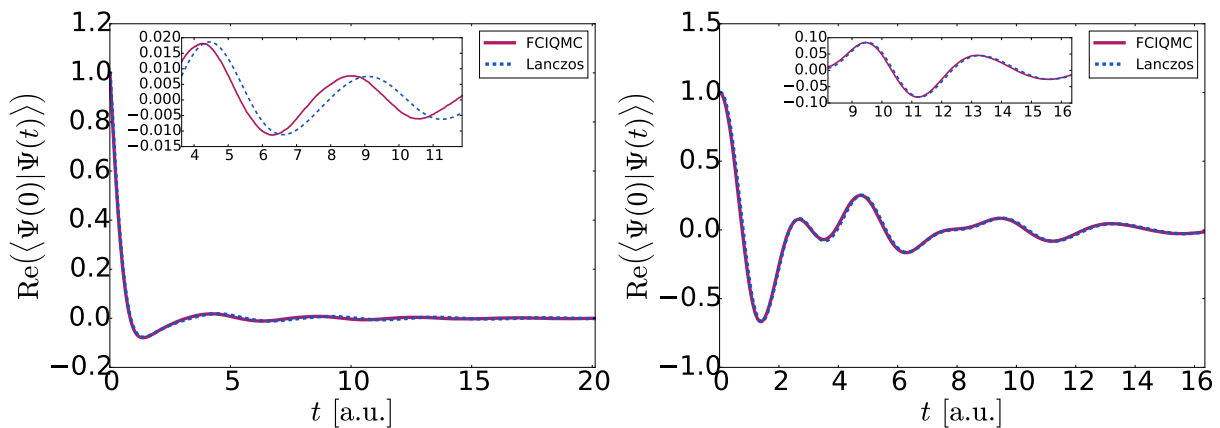
FIG. 7. Photoemission Green's function for $k = (0,0)$ for the Hubbard model with an 18-site cluster at $U/t = 2$ obtained with FCIQMC and Lanczos with a) 70000 and b) 17 million walkers, showing a bias in the Green's function due to under-sampling for the smaller walker number.

suppresses high-lying states (far from $\mu$) more than low-lying states, enhancing the relative weight of low-lying states, as the suppression scales with energy. The result is that low-lying states contribute to the Green's function over a longer time, and it then becomes easier to extract the information about these states. This should then also improve the signal to noise ratio for low-lying states. Fig. 10 (e.g., for $\alpha_0 = \pi/4$ or 0.2) illustrates how structures close to $\mu$ are described more accurately.

We can use

$$\mu = \begin{cases} E_0^{N+1}(\mathbf{k}) - E_0^N & \text{inverse photoemission} \\ E_0^N - E_0^{N-1}(\mathbf{k}) & \text{photoemission} \end{cases} \quad (30)$$

In this way the contribution to the spectrum from $|\Psi_0^{N\pm1}(\mathbf{k})\rangle$ is not damped by $\alpha(t)$, and its contribution to the spectrum is therefore well described.

Sometimes the lowest states of the $(N\pm1)$-system with a given $\mathbf{k}$ have little or no weight in the spectrum of interest and it may then be favorable to reduce (increase) $\mu$ even more for (inverse) photoemission. Eventually, however, these states obtain weight due to statistical noise and then grow exponentially. The shift of $\mu$ should therefore not be too large.

The Matsubara formalism has often been used to study the Mott metal-insulator transition or the formation of a pseudo gap. Then the (angular integrated) spectrum at $\mu$ is of particular interest, and the Matsubara formalism provides very useful information. However, we are often also interested in angular resolved spectra, where for a given $\mathbf{k}$ the leading peak may be located well away from $\mu$. Then the separate treatment of each $\mathbf{k}$ in the present formalism, and the related possibility to shift the spectrum, becomes particularly important. Satellites are also often of interest, and then the use of a relatively small $\alpha(t)$ in the FCIQMC is of great advantage.

In the Matsubara formalism the photoemission and inverse photoemission spectra are treated simultaneously.

In the $\mathbf{k}$-resolved case the relative weights, and thereby the relative standard deviations, may be very different. The present separate treatment of the two spectra then becomes an important advantage, since the relative standard deviations are comparable for the two spectra.

**The initiator approximation**

We make use of the initiator version of FCIQMC [20, 30] which is commonly used in the projective algorithm. This limits the possibilities for walkers to spawn to unoccupied determinants and thereby prevents sign errors from proliferating. The adaptation made is, that spawns onto unoccupied determinants are only accepted if they either came from a determinant exceeding a certain threshold occupation or if another spawn onto the same determinant occurred in the same iteration.

In contrast to the projective algorithm, the threshold value itself is not very significant for the purpose of Green's function calculation, as the initial wave function already has a high number of determinants populated, and only their population will enter the Green's function. Also, the event of two spawns occurring onto the same determinant is common, limiting the influence of the threshold further.

It can then be highly beneficial to either pick a high threshold, or entirely disable the possibility to spawn onto unoccupied determinants by single spawns and require two spawns to populate a new determinant. Fig. 8 shows the effect of the threshold onto the Green's function and the spectral function for exemplary cases. The effect on the Green's function is minor. For the $C_2$ molecule, the high-energy part of the spectrum exhibits some sensitivity, whereas the low-energy part notices only a constant shift which does not enter energy differences.
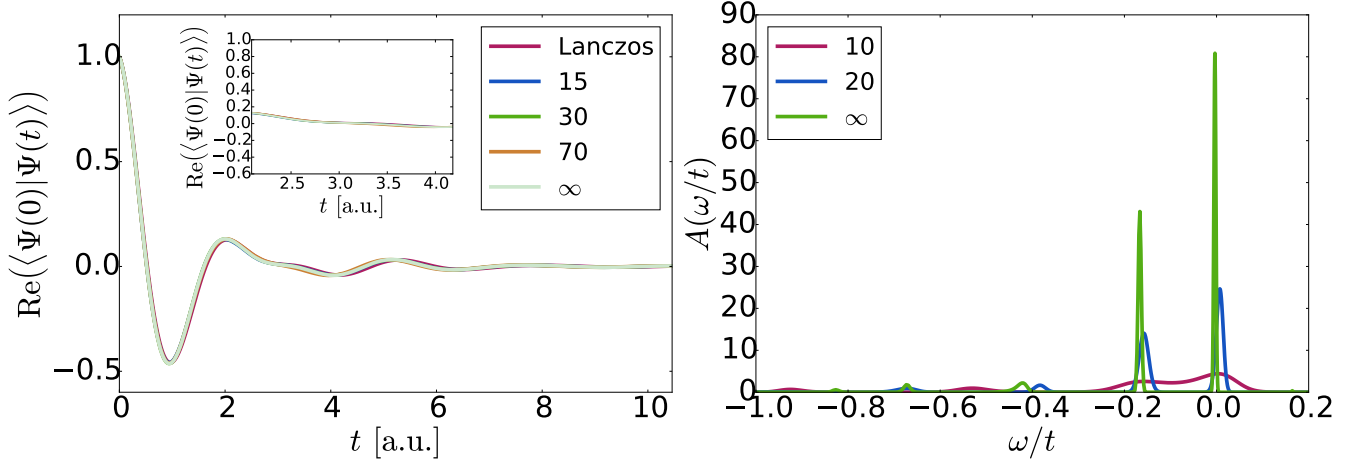
FIG. 8. (a) Green's function of the $U/t = 2$ 18-site Hubbard model for fixed $\alpha = 0.2$ for different initiator thresholds and without any initiators ($\infty$), allowing only double spawns to populate new determinants, and as obtained using Lanczos. (b) Photo absorption spectra of $C_2$ in the cc-pVTZ basis set for different thresholds and without initiators. Large values of $\alpha$ were used for the smaller thresholds, leading to broader spectra.

### Maximum entropy

The maximum entropy method [15, 16] for calculating spectral functions is often applied together with the finite temperature Matsubara formalism, where the spectral data are then analytically continued from the imaginary to the real axis. Here we develop a formalism for analytic continuation from an arbitrary path in the complex plane to the real axis, using the (inverse) photoemission spectrum as an example. The spectrum $A_{ij}(\omega)$ is related to the solution of the Schrödinger equation via

$$g_k = \sum_l K_{kl} a_l, \qquad (31)$$

where $g_k = \langle \Psi_i^\pm(0) | \Psi_j^\pm(t_k) \rangle$, $a_l = A_{ij}^\pm(\omega_l)$ and

$$K_{kl} = \exp\{-i \int_0^{t_k} dt e^{\mp i\alpha(t)} \omega_l\} f_l, \qquad (32)$$

where $f_l$ is a weight factor for the $\omega$ integration and the lower (upper) sign refers to (inverse) photoemission. The indices $i$ and $j$ have been dropped for simplicity. We introduce the average $\bar{g}_k$ over many samples of $g$ and define the deviation $\chi$ of a spectral function $a$ giving $g$ from $\bar{g}$ as

$$\chi^2 = \sum_{k=1}^L \sum_{k=1}^L (\bar{g}_k - g_k)^*[C^{-1}]_{kl}(\bar{g}_l - g_l). \qquad (33)$$

where the sums run over the $L$ values of $g_k$ and $C$ is the covariance matrix [15, 16] of the samples of $g$. To obtain a regular expression for $\chi^2$, it is important to have a non-singular covariance matrix $C$, as the inverse $C^{-1}$ is required to calculate $\chi^2$. If few samples are used, $C$

may be ill-behaved. We have then imposed a minimum value, $\sigma_{\min} \approx 10^{-4} \dots 10^{-6}$, on the diagonal entries of $C$. While this allows for regularizing $C$, it also assumes the data to be more noisy than it actually is and hence can affect the details of the spectra as illustrated in Fig. 9. Alternatively, we have split the data in batches and assumed a diagonal $C$ for each batch. This assumption can overemphasize noise, which tends to be compensated by averaging over batches.

We also introduce the entropy $S$

$$S = \sum_{i=1}^L [a_i - m_i - a_i \ln(a_i/m_i)] f_i, \qquad (34)$$

where $m_i$ is default function providing a guess for $A(\omega)$. We minimize $\chi - \gamma S$, where $\gamma$ determines the importance of the entropy. The most probable value of $\gamma$ is chosen [15, 16]. This leads to a system of nonlinear equations. This system is solved iteratively, by linearizing the equations around successive approximations $a_i^{(m)}$. We introduce $a_i^{(m+1)} = a_i^{(m)} + \delta a_i^{(m+1)}$ and solve

$$\sum_j \mathrm{Re}[K^\dagger C^{-1}]_{kj} \bar{g}_j - \sum_{jl} \mathrm{Re}[K^\dagger C^{-1} K]_{kl} a_l^{(m)}$$

$$-\gamma \ln \frac{a_k^{(m)}}{m_k} = \sum_l \Lambda_{kl}(a_k^{(m)}) \delta a_l^{(m+1)}. \qquad (35)$$

where

$$\Lambda_{kl}(a_k^{(m)}) = \{ \frac{f_k \gamma}{a_k^{(m)}} \delta_{kl} + \mathrm{Re}[K^\dagger C^{-1} K]_{kl} \} \qquad (36)$$

Fig. 10 show results for the Hubbard model with four different $\alpha(t) \equiv \alpha_0$. The spectrum was obtained from exact diagonalization, transformed to complex $t$ and Gaus-
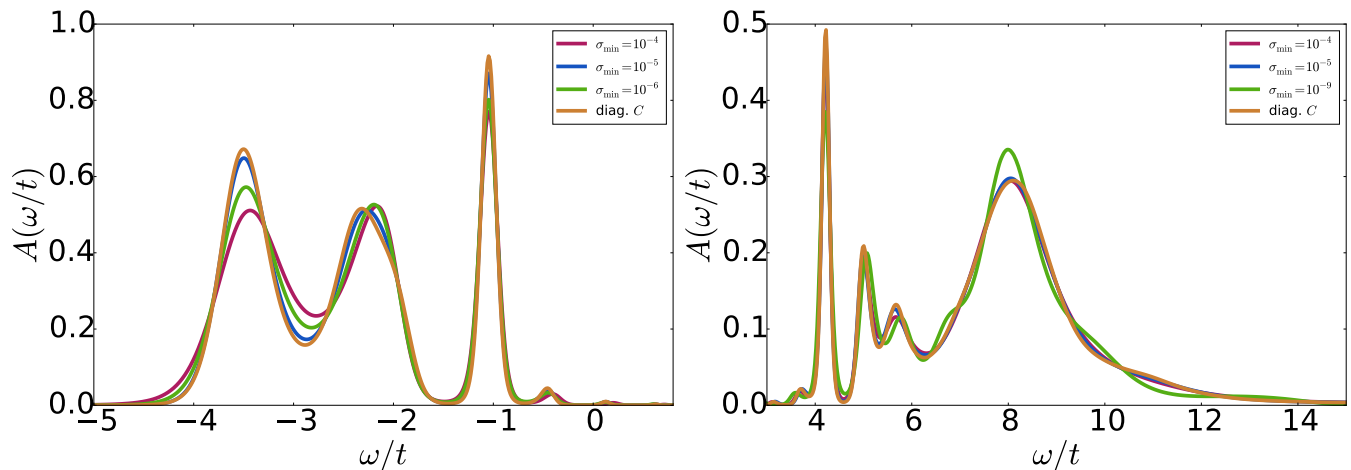
FIG. 9. Spectra obtained using maximum entropy obtained using different values of the cutoff $\sigma_{\min}$ for the photoemission (left) and the inverse photoemission of the 22-electron 24-site (right) Hubbard model at $U/t = 4$. While the photoemission spectrum shows sensitivity to the cutoff, the inverse photoemission spectrum does not as long as the covariance matrix is non-singular. For $\sigma_{\min} = 10^{-9}$, this is no longer the case here and the analytic continuation is ill-defined, leading to deviations in the spectrum. For comparison, the spectrum obtained by partitioning the data in 6 batches, assuming a diagonal $C$ and averaging over the spectra obtained from each batch is also shown.

sian noise was added. The spectrum was then transformed back to real frequencies using maximum entropy and compared with the exact result. For data on the imaginary axis ($\alpha_0 = \pi/2$), the $\omega = 0$ peak is accurately described, while the other structures are approximated by two peaks. For data close to the real axis ($\alpha_0 = 0.1$) almost all structures are reproduced.

To understand what accuracy can be obtained, we expanded the work in Ref. 39 and introduce the eigenvectors $|\nu\rangle$ and eigenvalues $\varepsilon_\nu$ of $\Lambda$. We expand the differences $\delta a = a - a_{\text{exact}}$, $\delta m = m - a_{\text{exact}}$ and the stochastic error in $\bar{g}$ in the eigenvectors $|\nu\rangle$ and obtain coefficient $\delta a_\nu$, $\delta m_\nu$ and $\delta g_\nu$, satisfying

$$\delta a_\nu = \frac{1}{\varepsilon_\nu}(\delta g_\nu + \delta m_\nu). \tag{37}$$

Typically there are several very large $\varepsilon_\nu$. The corresponding components of $a$ are then very accurately described. Other eigenvalues are approximately unity, and the corresponding $\delta a_\nu$ cannot be trusted.

The bottom of Fig. 10 shows the eigenvectors for $\alpha_0 = \pi/2$ and $\pi/4$. The eigenvalues for $\alpha_0 = 1$ are

$2 \times 10^6$, $3 \times 10^4$, $5 \times 10^3$, 73, 5. The components of $A(\omega)$ corresponding to the first four or five eigenvectors are then described very well. These eigenvectors do not have enough nodes to describe details away from $\omega = 0$. As $\alpha_0$ is reduced the number of eigenvalues larger than 5 increases from 10 ($\alpha_0 = \pi/4$) or 20 ($\alpha_0 = 0.2$) to about 40 ($\alpha_0 = 0.1$). Correspondingly, more and more details of the spectrum can be described. The $|\nu\rangle$ and $\varepsilon_\nu$ help us judge which details of $A(\omega)$ can be described and which cannot.

### Additional Data

In addition to the study on the half-filled 18-site Hubbard model with $U/t = 2$, calculations on the same system with $U/t = 4$ have been performed, of which the resulting spectra are displayed in Fig. 11.

For completeness, we also consider the Carbon dimer in a minimal cc-pVDZ basis set consisting of 14 orbitals per atom in the frozen core approximation. The Hilbert space size here is $\sim 10^8$, and photo absorption spectra can be obtained analogously to the basis sets described in the main text, which are shown in Fig. 12.
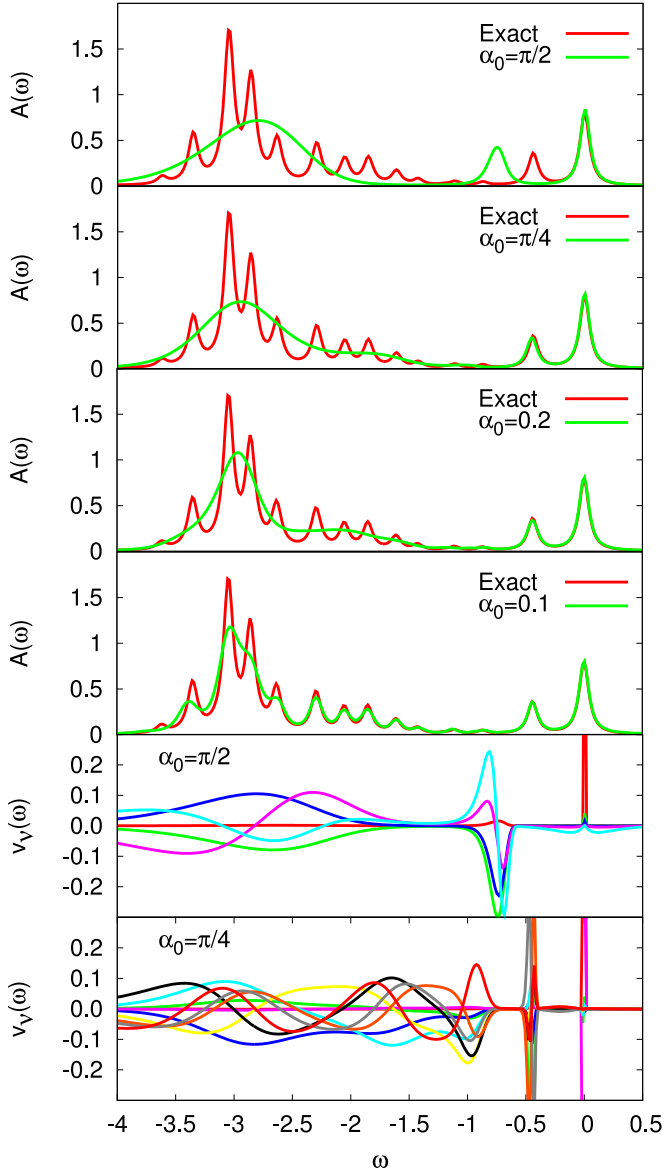
FIG. 10. Photoemission spectrum for the Hubbard model with 18 sites, $U/t = 8$ for different functions $\alpha(t) \equiv \alpha_0$ (top four figures). The bottom two figure shows the basis functions $|\nu\rangle$ with $\varepsilon_\nu > 5$ for $\alpha_0 = \pi/2$ and $\pi/4$. The chemical potential is chosen so that one peak is at $\omega = 0$. The data have Gaussian noise with a relative standard deviation of about $10^{-2}$. The spectra have been given a Lorentzian broadening with FWHM=0.1.
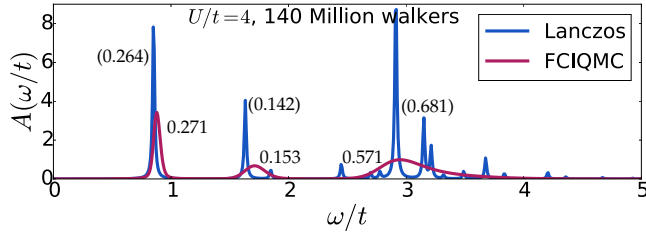
FIG. 11. Spectrum for the 18-site half-filled model at $U/t = 4$ obtained with $1.4 \times 10^8$ walkers for $k = (0,0)$. Both the integrated weights of the peaks of the FCIQMC spectrum as well as the corresponding integrated weights of the Lanczos spectrum (bracketed) are displayed, showing reasonable agreement.
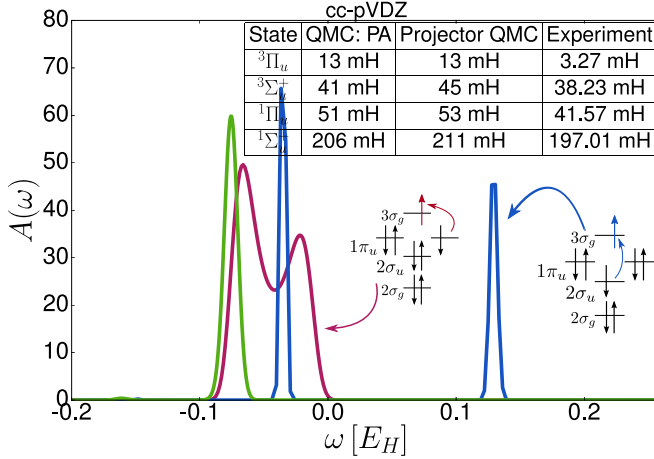


| State | QMC: PA | Projector QMC | Experiment |
|-------|---------|---------------|------------|
| $^3\Pi_u$ | 13 mH | 13 mH | 3.27 mH |
| $^3\Sigma_u^+$ | 41 mH | 45 mH | 38.23 mH |
| $^1\Pi$ | 51 mH | 53 mH | 41.57 mH |
| $^1\Sigma$ | 206 mH | 211 mH | 197.01 mH |

FIG. 12. Photo absorption spectra for the Carbon dimer in a cc-pVDZ basis set for a single excitation from the $2\sigma_u$(blue)/$1\pi_u$(red) to the $3\sigma_g$ orbital. Next to the real-time FCIQMC estimates of the excitation energies we also list the corresponding energies as obtained using excited-state i-FCIQMC method [27] and the FCIQMC ground state energy from [28]. The time step used is $\Delta t = 5 \times 10^{-3}$. Again, a rotation of time in the complex plane is performed, with an angle of $\alpha \sim 0.33$, which is higher than for the larger basis sets due to the larger time-step, leading to an increased broadening.